

Optical, Morphological and Microstructural Investigation of TiO₂ nanoparticles for Photocatalytic application

B. Manikandan^a, K. R. Murali^b and Rita John^{a*}

a) Department of Theoretical Physics, University of Madras, Chennai-600 025, India

b) Electrochemical Material Science Division, CSIR- Central Electrochemical Research Institute, Karaikudi, India

Received 29 June 2020; received in revised form 27 February 2021; accepted 28 February 2021

ABSTRACT

Enriched characteristics like porosity, stability and specific surface area assist TiO₂ to find extensive applications in photocatalysis, dye sensitized solar cell, and sensors. TiO₂ semiconductor was prepared using titanyl acetylacetonate and characterized by XRD, FTIR, Raman, UV-Vis, FESEM, EDX, and DLS. XRD result confirmed the tetragonal structured anatase TiO₂ semiconductor. Scherrer formula is used to calculate crystallite size and the obtained value is 6.81 nm. Microstrain, stress, energy density, and crystallite size are calculated using W-H model. The absorption peak of TiO₂ is observed at 652.11 cm⁻¹ from FTIR spectrum and authenticated the anatase TiO₂ semiconductor. The UV absorption edge is identified at 365 nm and the bandgap is calculated from the Kubelka-Munk equation using Tauc plot. Raman spectrum show bands at 140, 197, 395, 512, and 635 cm⁻¹ and these peaks confirmed the presence of the anatase TiO₂ stretching mode. FESEM micrographs exhibited agglomerated spherical morphology and the particle size was further analysed using DLS study. The elemental compositions were identified in the EDX analysis. The obtained spectrum showed 55.88 Wt% of O and 44.12 Wt% of Ti atoms. The prepared anatase TiO₂ semiconductor indicated enhanced catalytic behaviour. The rate constants and half life time are related to crystallite size using mathematical relation. It is found that the degradation process varies with crystallite size.

Keywords: TiO₂, Sol-Gel; XRD; Strain; UV-Vis; Photocatalysis

1. Introduction

Wastage from textile industries contain various toxic dyes. It causes environmental problems harmful to human life and other biological species [1] when the polluted molecules pass into the water resources. It is essential to degrade pollutants to safeguard the environment and human life from various diseases that are caused by these effluent toxic dyes. Advanced oxidation processes are involved in heterogeneous photocatalysis, where the mineralization of pollutants could be achieved using a suitable catalyst under UV or Visible light irradiation. In this process, hydroxyl and superoxide radicals are generated, which play an important role in the degradation of pollutants [2]. In the photocatalysis process the redox reactions take place at the interface between the semiconductor and polluted dye. When light energy irradiated on semiconductor ($h\nu \geq E_g$) the electron (e_{CB}^-) hole (h_V^+) pairs are generated due to absorption of photons and the generat-

-ed holes can oxidize water molecule into hydroxyl (HO^\bullet) radicals. Similarly, the photo generated electrons produce the superoxide radical anion ($O_2^{\bullet-}$) when adsorbed by O_2 molecule. These radicals give non-toxic H_2O and CO_2 when it reacts with the pollutant molecules [3,4].

Semiconductors are the materials to be potentially used in different environmental and energy applications due to their advantageous optoelectronic properties [5,6]. In recent years, materials such as ZnO, TiO₂, SnO₂, Nb₂O₅ and NiO have attracted the attention of researchers [7–11]. These semiconductors play a significant role in photocatalysis and photonic devices [12–14]. Most of the semiconductors mentioned above are unstable, toxic, and corrosive under light illumination [15]. Comparing these semiconductors, TiO₂ has been studied extensively due to its low cost, availability, nontoxicity, strong oxidation capacity of photo generated charge carrier, high chemical, and photo stability [16]. These properties are important for various applications such as

*Corresponding author:

E-mail address: ritajohn.r@gmail.com (R. John);

photo catalysis [17,18], solar cells [19], sensors [20,21], and biomedical applications [22]. However, there is a need to explore TiO₂ semiconductor owing to its poor dye adsorption, lower surface area and charge recombination which is inhibiting the TiO₂ to become the best photocatalyst [23]. TiO₂ is an important semiconductor material for photocatalytic studies following the seminal work by Fujishima and Honda in 1972 [24]. It exhibits an important role as photocatalysis in water splitting [25,26], CO₂ reduction, photodegradation, organic reforming and water desalination: to solve the environmental issues [27,28]. In recent years TiO₂ is used in various practical applications in respect to the environment and energy.

TiO₂ material occurs in different forms such as rutile, anatase and brookite. Comparing these brookite phase is unstable whereas the other two are found to be the stable phases [29,30]. However, the anatase phase has favourable properties, which has been focused by many researchers over the last decades due to its applications in photodegradation and photovoltaic devices [31–33]. The structural and optical properties are important for various light energy dependent phenomenon and in this aspect, research is actively engaged in investigating TiO₂ semiconductor. TiO₂ nanoparticles are synthesized by various techniques [34] such as co-precipitation method [35,36], hydrothermal method [37,38], microemulsion [39], chemical bath deposition [40], sol-gel [41–43], and spray pyrolysis methods [44,45]. Among these, sol-gel method is the simplest route to synthesize nanoscale materials as it has the merits of homogeneity and control over temperature. Also this method requires simple equipment and is cost effective [46]. The structural and optical properties of sol-gel synthesized TiO₂ were characterized using different techniques. The XRD data are used to calculate various structural and surface parameters such as crystallite size, dislocation density, lattice constants, interplanar spacing, unit cell volume, density, number of unit cells in a particle, strain, specific surface area and porosity. In the past, crystallite size of TiO₂ was calculated using Scherrer's formula, while only a very few reports are available on the estimation of crystallite size based on Williamson-Hall model (W-H) for TiO₂ nanostructure [47]. W-H method is a simple method to analyse various physical properties such as crystallite size and lattice strain. These parameters have effective impact on intensity, peak width, and shift in Bragg's angle [48,49]. The strain and crystallite size relations were correlated through Williamson – Hall model [50,51]. In addition to this, catalytic performance of TiO₂ was studied with methylene blue and mathematical relations are used to evaluate the variations of rate constant with respect to

crystallite size. The photodegradation correlates with porosity, specific surface area, and crystallite size.

2. Experimental

2.1. Materials

For typical synthesis process, the following chemicals are used: Titanyl acetylacetonate (Merck, 99.5% Purity), Ethanol (Analytical Reagent, 99.9% purity) and Deionised water (Laboratory Reagent).

2.2. Preparation

1.31 g of titanyl acetylacetonate was added to 50 mL of ethanol and stirred for 40 min with a magnetic stirrer at 60 °C temperature. The pH value of the solution was measured to be around 5. The hydrolysis and condensation processes were initiated. pH was adjusted by adding 10 mL of deionised water drop by drop while maintaining the temperature at 80 °C. The sol solution was again stirred for 3 hours to obtain the consistency of a homogenous gel. The gel was left to age overnight and washed several times with ethanol and distilled water. The obtained gel was dried and ground with agate mortar. Finally, it was annealed at 500 °C for 4 hours.

2.3. Characterization techniques

Powder X-ray diffractometer (SEIFERT JSO2002) equipped with monochromatic CuK α_1 radiation ($\lambda=0.15406$ nm) was used to confirm the crystalline nature of prepared material. FTIR spectrum was recorded in the range 400-4000 cm⁻¹ by Bruker Fourier Transform Infrared Spectroscopy. Raman spectroscopy (Nanophoton Raman-11, Japan) was used for Raman spectrum analysis of TiO₂ nanoparticles. The optical properties were analysed using UV-Vis-NIR spectrometer (Varian, model 500). FESEM (model: HITACHI SU6600) was used to examine morphology and elemental composition of the prepared material. DLS technique was used for particle size measurements using a Malvern Zeta sizer instrument (ZEN3600).

2.4. Photocatalytic degradation

The reaction beaker was illuminated from a distance of 6 cm with Philips UV light (2 × 15 W UV tube, 365 nm) at room temperature. The degradation of MB dye was performed as follows; 20 mg of TiO₂ catalyst was dispersed in 100 mL of MB aqueous solution. The pH of the solution was maintained to be 10. The solution was stirred continuously at a stirring rate of 1000 rpm to eliminate external mass. Before irradiating the solution mixture with UV light, the suspension was stirred at the rate of 800 rpm in the dark for 30 minutes. This is done to establish the adsorption/desorption equilibrium of MB. The aqueous samples were centrifuged to remove

the suspended solid catalyst particles. The residual concentration of MB was measured at 665 nm using the UV-Vis spectrophotometer (Perkin-Elmer lambda 650 nm) in liquid cuvette configuration with de-ionized water as reference.

3. Result and Discussion

3.1. Structural analysis

The synthesized TiO₂ nanoparticles were analysed for structural properties using X-ray diffraction and the obtained XRD pattern is shown in **Fig. 1**. The peaks at 25.35° (101), 37.75° (004), 48.07° (200), 53.78° (105), 54.86° (211), 62.74° (204), and 68.98° (116) clearly show the presence of tetragonal anatase TiO₂ structure and its good crystalline nature. The highest intensity peak at 2θ=25.35° was found with (101) orientation. The obtained peak values match well with standard JCPDS# 21-1272. The Scherrer formula was used to calculate the crystallite size, which is given in following equation (1).

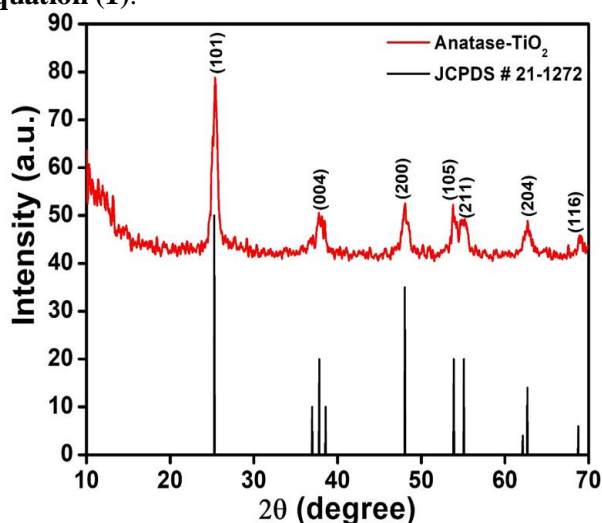


Fig. 1. The XRD pattern of anatase-TiO₂ nanoparticle

$$\text{Crystallite Size } (D) = \frac{K\lambda}{\beta \cos \theta} \quad (1)$$

where, D is the crystallite size in nm, K is the shape factor which is equal to 0.94, λ is the wavelength of X-ray radiation Cu k_{α1} (λ = 1.5406 Å), β is full width half maximum intensity (FWHM), and θ is the Bragg's angle.

The average crystallite size obtained is 16.81 nm. The smallest crystallite size is found to be in (101) plane compared to other planes because of the presence of high intensity and broadened peak. It is observed that the crystallite size depends on various factors such as intensity, peak broadening, sharpness, dislocation density, and strain. The dislocation density (δ), lattice constants (a and c), interplanar spacing (d), unit cell volume (V), density (ρ), number of unit cells in a particle (n), and strain (ε) were calculated by using equations (2-7). The calculated values are given in **Tables 1 and 2**.

$$\text{Dislocation density } (\delta) = \frac{1}{D^2} \quad (2)$$

$$\text{Inter-planner spacing } \frac{1}{d_{(hkl)}^2} = \left(\frac{h^2 + k^2}{a^2} \right) + \frac{l^2}{c^2} \quad (3)$$

$$\text{Volume } (V) = a^2c \quad (4)$$

$$\text{Density } (\rho) = \frac{nM}{NV} \quad (5)$$

$$\text{Number of unit cells in a particle } (n) = \frac{4}{3\pi \left(\frac{D}{2v} \right)} \quad (6)$$

$$\text{Strain } (\epsilon) = \beta_{hkl} / (4 \tan \theta) \quad (7)$$

where; D is crystallite size, M is molecular weight, N is Avogadro number, V is unit cell volume, n is 2 for rutile phase and 4 for anatase phase.

Table 1. The obtained crystallographic parameters from XRD characterization

2θ (degree)	(hkl)	FWHM β(degree)	FWHM (Radian)	Crystallite size D (nm)	d- Spacing (Å)	Dislocation density δ x10 ⁻³	Strain (ε)
25.35	(101)	0.6041	0.01054	13.46	3.5165	5.5196	0.01172
37.75	(004)	0.5270	0.00919	15.87	2.3785	3.9705	0.00672
48.07	(200)	0.5046	0.00886	17.25	1.8922	3.3606	0.00498
53.78	(105)	0.5185	0.00904	17.07	1.7001	3.4319	0.00446
54.86	(211)	0.4839	0.00844	18.44	1.6663	2.9409	0.00407
62.74	(204)	0.3600	0.00628	25.75	1.4808	1.5082	0.00258

Table 2. The calculated average value of various parameters

Parameter	Calculated values
Average Crystallite size (D)	16 nm
Average Dislocation density (δ)	3.7684×10^{-3}
Lattice constant (\AA)	$a=3.7845, c= 9.5136$
Unit cell volume (V)	$136.26 (\text{\AA})^3$
Density (ρ)	$3.7695 (\text{g cm}^{-3})$
Porosity (P)	42.70%
Specific surface area (SSA)	$91.97 (\text{m}^2/\text{g})$
Number of unit cell in particle (n)	6
Strain (ϵ)	0.6718×10^{-3}

The porosity and specific surface area were also calculated using following formula **equations (8 and 9)**;

$$\text{Porosity} = \left(1 - \frac{n_p^2 - 1}{n_w^2 - 1}\right) \times 100\% \quad (8)$$

$$\text{Specific Surface Area (S)} = \frac{6000}{D\rho} \quad (9)$$

where; D is the crystallite size, S is the specific surface area, ρ is the density of anatase TiO_2 nanoparticles, n_p and n_w are refractive indices of the porous and pore free anatase structure ($n_w = 2.52$), respectively [52–54].

The linear relationship between density and refractive index are given in **equation (10)**, which gives the refractive index of porous anatase TiO_2 [55].

$$\text{Relation between density and refractive index } (\rho) = - \frac{n_p - 0.91933}{0.42275} \quad (10)$$

Fig. 2 and **Fig. 3** indicate the variation of crystallite size with dislocation density and strain present in the material. The dislocation density is due to irregularity or cracks in the crystal structure. The increase in dislocation density increases the strain which in turn decreases the crystallite size. The result showed in **Figs. 2** and **3** endorses that the crystallite size is directly related to strain and dislocation density. The peak shift or the peak broadening depends on the strain present in the materials. In general, peak shift refers to homogenous strain and peak broadening to inhomogeneous strain. The peak broadening in turn reduces the crystallite size. The broadening stops increasing, when strain reached a certain limit which is known as inherent instrumental broadening ($\beta_{\text{instrument}}$). **Fig. 3b** shows the strain induced instrumental peak broadening (β_D) effect on crystallite size. The result infers that the crystallite size decreases as strain increases up to 0.0069, beyond which the crystallite size tends to increase which is shown in inset in **Fig. 3b**. This confirms that the crystallite size could be larger for

higher strain present in the crystallite structure. This is further confirmed by the Williamson-Hall model.

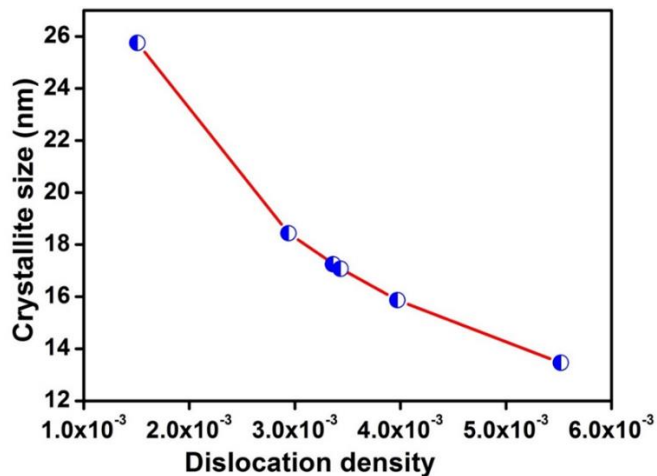


Fig. 2. The variation of crystallite size with dislocation density

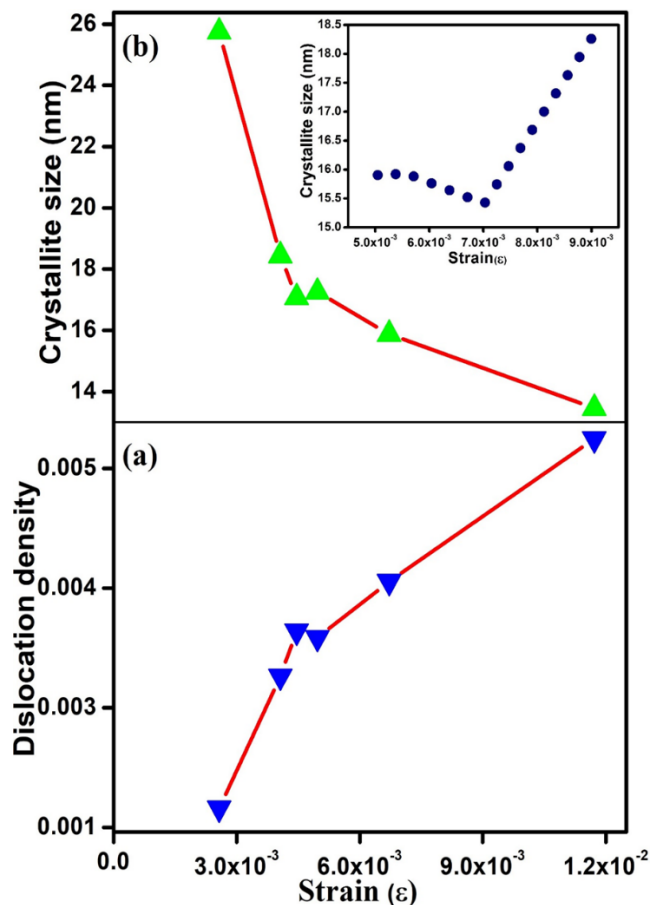


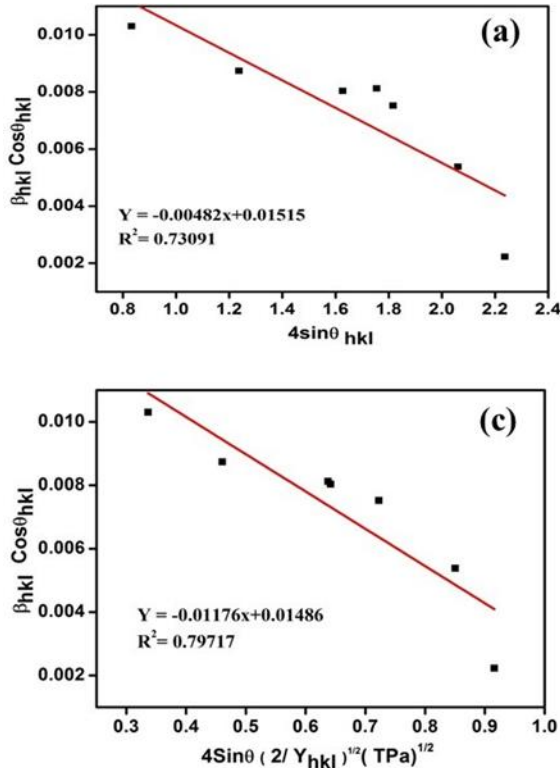
Fig. 3. Effect of strain: a) Strain vs. Dislocation density b) Strain vs. crystalline size

3.2 Williamson-Hall model

As mentioned above the crystallite size is effectively influenced by strain which is reflected in the line broadening along (101) plane in the XRD pattern. The

reason for this strain induced line broadening is due to the presence of distortions in the crystal structure. The relationship between the crystallite size and strain is given by the Williamson-Hall model in **equation (11)**. The peak width depends on the instrumental factors, different strain and with the presence of defects in the lattice [56]. The W-H equation can be modified into **equation (12)** when the crystallite size and strain become independent.

$$\beta_{hkl} = \beta_D + \beta_\epsilon \quad (11)$$



$$\beta_{hkl} \cos \theta_{hkl} = \frac{K\lambda}{D} + 4\epsilon \sin \theta_{hkl} \quad (12)$$

where, β_D and β_ϵ are contributions from crystallite size and strain respectively. β_{hkl} is instrumental corrected broadening.

The obtained results and calculated values are shown in **Fig. 4** (a-d) and **Table 3**. The interrelation between crystallite size and strain is shown in **Fig. 5**. The plot clearly confirms that the crystallite size increases as strain increased in the material.

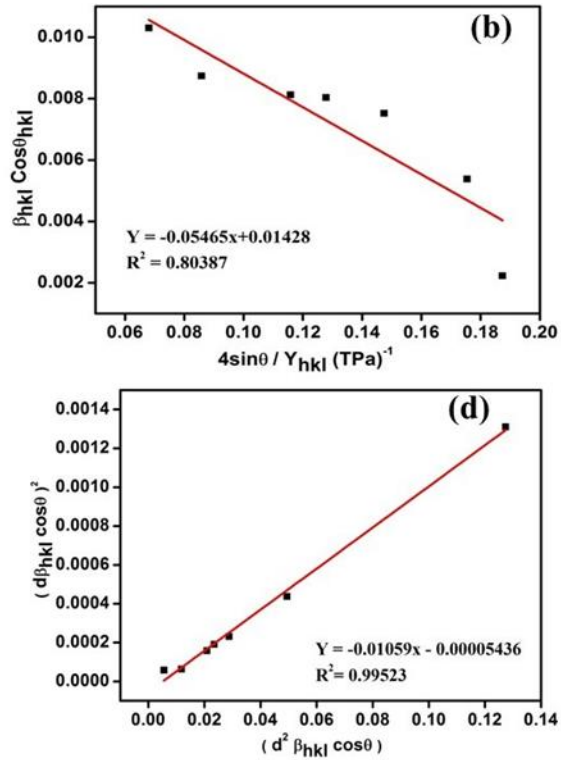


Fig. 4. Williamson-Hall analysis: a) Plot for $\beta_{hkl} \cos \theta$ vs $4 \sin \theta$ b) Plot for $\beta_{hkl} \cos \theta$ vs $4 \sin \theta / Y_{hkl}$ c) Plot for $\beta_{hkl} \cos \theta$ vs $4 \sin \theta \left(\frac{2}{Y_{hkl}} \right)^{1/2}$ d) Plot for $(d_{hkl}^2 \beta_{hkl} \cos \theta)^2$ vs $(d_{hkl} \beta_{hkl} \cos \theta)^2$

Table 3. The crystallite size and physical parameter of anatase TiO_2 from XRD data.

Scherer Method		Williamson- Hall (W-H) method						Size-Strain Plot (SSP)					
D nm	ϵ $\times 10^{-3}$	UDM		USDM			UEDDM				D_V nm	ϵ_a $\times 10^{-3}$	ϵ_{RMS} $\times 10^{-3}$
		D nm	ϵ $\times 10^{-3}$	D nm	ϵ $\times 10^{-3}$	σ MPa	D nm	ϵ $\times 10^{-3}$	σ MPa	u_{ed} KJm^{-3}			
17.31	0.67	15.15	4.82	14.28	4.21	54	14.86	4.26	55	117.6	106	0.14	0.054

3.3 FTIR analysis

The FTIR spectrum range of 400-4000 cm^{-1} (**Fig. 6**) confirms the presence of stretching and bending vibrations of Ti, and O atoms, as well as functional groups. The FTIR spectra contains two regions being functional groups and finger print regions. Where the

fingerprint region gives the presence of absorption bands of oxides. The significant band at 652.11 cm^{-1} is associated with anatase TiO_2 metal oxide [59]. The absorption peak around 1363.60 cm^{-1} and 1634.29 cm^{-1} are due to the stretching and bending vibrations of water molecule [60]. The peak at 3381.24 cm^{-1} is due to the surface adsorbed hydroxyl groups and the band located

at 2923.42 cm^{-1} is attributed to the C-H stretching vibration [61]. The obtained results clearly show the presence of Ti-O stretching mode, water molecule, and OH groups.

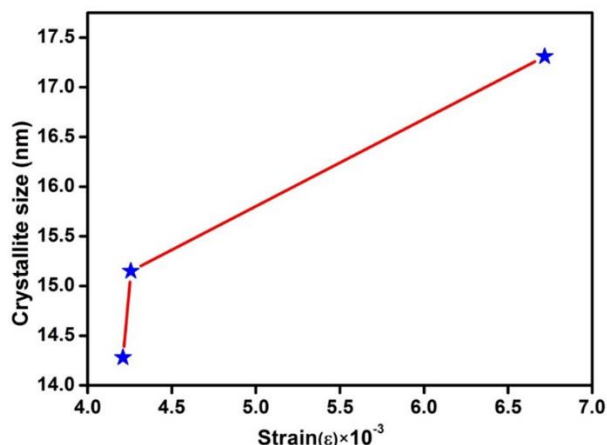


Fig. 5. The variation of Crystallite size with Strain

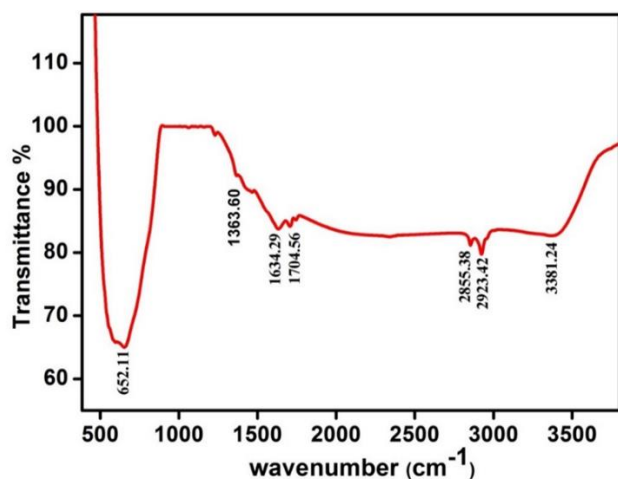


Fig. 6. FTIR spectrum of TiO₂ nanoparticles

3.4 Optical analysis

Fig. 7 shows the absorption spectrum of prepared TiO₂. The absorption edge was observed at 365 nm and confirm the activity in UV region. The optical band gap was calculated from the Kubelka-Munk equation (13) using Tauc's relation, which is a plot between $h\nu$ (eV) and $(\alpha h\nu)^{1/2} (\text{cm}^{-1} \text{eV})^2$.

$$(\alpha h\nu) = C (h\nu - E_g)^n \quad (13)$$

where, E_g is the band gap (eV), $h\nu$ is the energy of incident photons (h Planck's constant in J s, ν the light frequency in s^{-1}), β presents the absorption constant, α presents the absorption coefficient (by the Beer-Lambert's law as $\alpha = ([2.303 \times \text{Abs}]/d)$, where d and abs. are the sample thickness and sample absorbance, respectively) [62] and n depends on the type of transition [61]. The transition values of direct, indirect, forbidden direct and forbidden indirect bands are 1/2, 2,

3/2 and 3 respectively. The band gap determined from the plot between $h\nu$ and $(\alpha h\nu)^{1/2}$ is 3.18 eV.

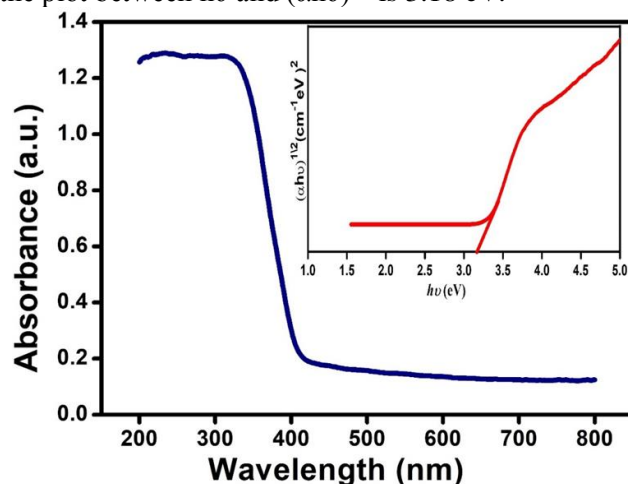


Fig. 7. Absorption spectrum and Tauc plot (Inserted) of TiO₂ nanoparticles

3.5 Raman analysis

The Raman spectrum of anatase TiO₂ is shown in Fig. 8. It has a tetragonal structure and belongs to the space group $D_{4h}^{19} = (I4/amd)$ with two TiO₂ formula units per primitive cell [63]. According to factor group analysis, anatase TiO₂ has 15 optical modes with the irreducible representation, $1A_{1g} + 1A_{2u} + 2B_{1g} + 1B_{2u} + 3E_g + 2E_u$. In the representation, A_{1g}, B_{1g}, E_g are Raman active modes, A_{2u}, E_u are infrared active modes and B_{2u} mode is inactive for both Raman and infrared. The Raman peaks were observed at 140, 395, 512, and 635 cm^{-1} which can be attributed to $E_g, B_{1g}, A_{1g},$ and E_g symmetry modes of anatase TiO₂, respectively [64]. The first E_g peak at 140 cm^{-1} is a characteristic peak of anatase TiO₂, this intense peak is influenced by crystallite size of anatase TiO₂ which shows blue shift with increasing line width and decreasing crystallite size. The peak is slightly broader which is due to either surface pressure or phonon confinement effect [65].

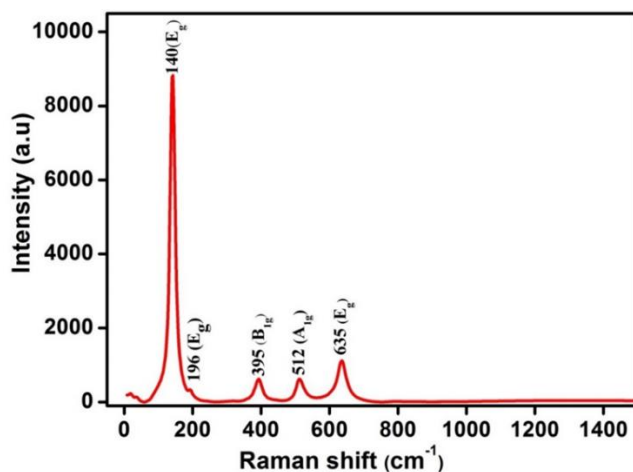


Fig. 8. Raman spectrum of TiO₂ nanoparticles

3.6 Morphological study

Fig. 9 shows the surface morphology of anatase TiO₂ by Field Emission Scanning Electron Microscopy (FESEM). The FESEM analysis was taken at different magnifications and the micrographs indicate agglomerated spherical shape particles. The elemental composition was carried out using energy dispersive X-ray analysis (EDX). The obtained spectrum is shown in **Fig. 10**, which exhibits Ti (44.12%) and O (55.88%) peaks in the prepared anatase TiO₂ nanostructure. **Fig. 11** shows the particle size distribution obtained by dynamic light scattering (DLS) using Malvern Zetasizer. The obtained particle size is 1057 nm and is found to be bigger than the particle size obtained by FESEM. The possible reason for the difference in particle size is due to the agglomeration effect of nanoparticle [66,67].

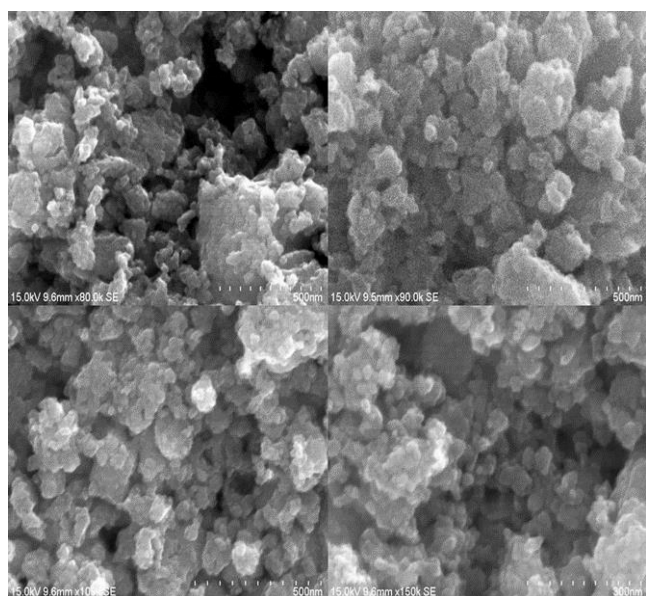


Fig. 9. Morphology of TiO₂ nanoparticles

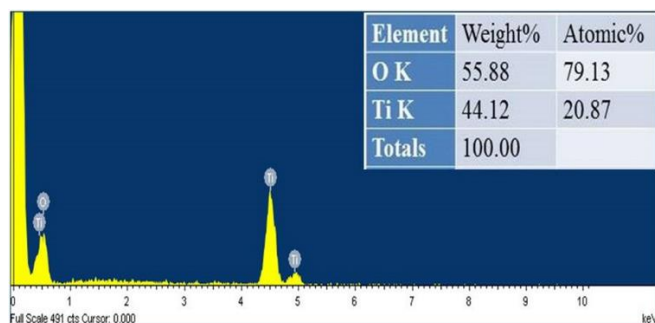
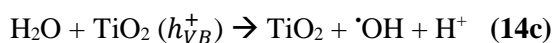
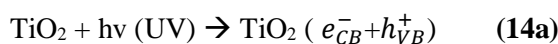


Fig. 10. EDX Spectrum of TiO₂ nanoparticle

3.7 Photocatalytic activity

Photocatalytic study was carried out using UV light illumination on MB dye with TiO₂ as the catalyst. Methylene blue dye causes many environmental problems due to its hazardous nature [68]. TiO₂

nanoparticles show better degradation efficiency for methylene blue dye owing to its high porosity, surface area, highly crystalline, and effective generation of electrons-holes pairs [69,70]. The anatase TiO₂ photocatalyst gives electrons and holes when irradiated with UV light. The holes generated in the valance band, creates [•]OH from water and electrons in the conduction band creates O₂⁻ which degrades the dye [70,71]. The schematic representation of this process is given in **Fig. 12** and **equations 14 (a-e)**.



The effectiveness of TiO₂ to degrade MB dye was studied by varying irradiation time and repeating the cycling process. The degradation efficiency was calculated using **equation (15)** and obtained values are shown in **Table 4**.

$$\text{Degradation} = \left[\frac{C_t - C_0}{C_0} \right] \times 100 \quad (15)$$

where; C₀ is the initial concentration, C_t is the residue concentration after time 't' of photodegradation.

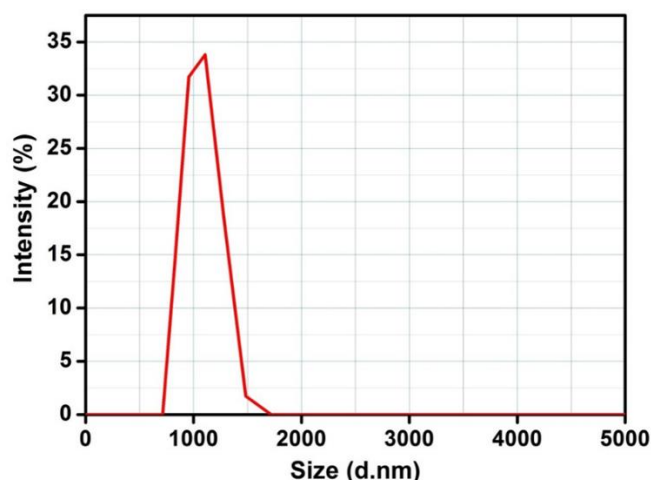


Fig. 11. Particle Size Distribution

Table 4. Degradation percentage and ln(C₀/C_t) values of Methylene blue (MB) dye with TiO₂ nanoparticles.

Time (min)	Degradation (%)	ln (C ₀ /C _t)
30	37.5	0.470004
60	56.2	0.825536
90	68.7	1.161552
120	88.7	2.180367
150	93.5	2.733368
180	95.1	3.015935

Fig. 13 (a-c) shows the results obtained from the photocatalytic process. **Fig. 13a** represents the behaviour of dye concentration with respect to time. It shows that the entire photo degradation process was completed within 180 minutes. **Fig. 13b** shows the degradation rate of MB for different cycles. The results clearly show that 120 min were taken for 90% degradation and it increases to 95% when degradation is allowed up to 180 min. This result indicates that synthesized TiO₂ is a suitable catalyst for MB dye. The calculated photocatalytic parameters are given in **Table 5**. The radicals in the photocatalytic reaction are responsible for degradation, which is correlated to the rate constant and half -life time. The higher rate constant and lower half-life time influence the kinetics of degradation. The kinetic behavior of degradation can be interpreted by the Langmuir–Hinshelwood equation, but only when the photodegradation is in equilibrium process. In kinetic point of view, the adsorption of both the oxidant and the pollutant is a pivotal parameter in a

heterogeneous photodegradation process [72]. The L-H relation is given in **equation (16)** and we can modify into logarithmic form (**equation 17**) by integrating **equation (16)**, which is similar to an apparent first-order equation.

$$r = \frac{-dc}{dt} = \frac{k'KC}{1+KC} = k'\theta \quad (16)$$

$$\ln\left(\frac{C_0}{C_t}\right) + k'(C_0 - C_t) = k'Kt = k_{app}t \quad (17)$$

where, *r* is the degradation rate of the reactant (mg/L min), *C* is concentration of the pollutant (mg/L), *t* is irradiation time, *k'* is specific reaction rate constant (mg/L min), *K* is equilibrium constant of the reactant (L/mg), *C*₀ is initial concentration, *C*_{*t*} is final concentration, and *k*_{*app*} is first-order rate constant, which is given by the slope of the graph: $\ln\left(\frac{C_0}{C_t}\right)$ versus time.

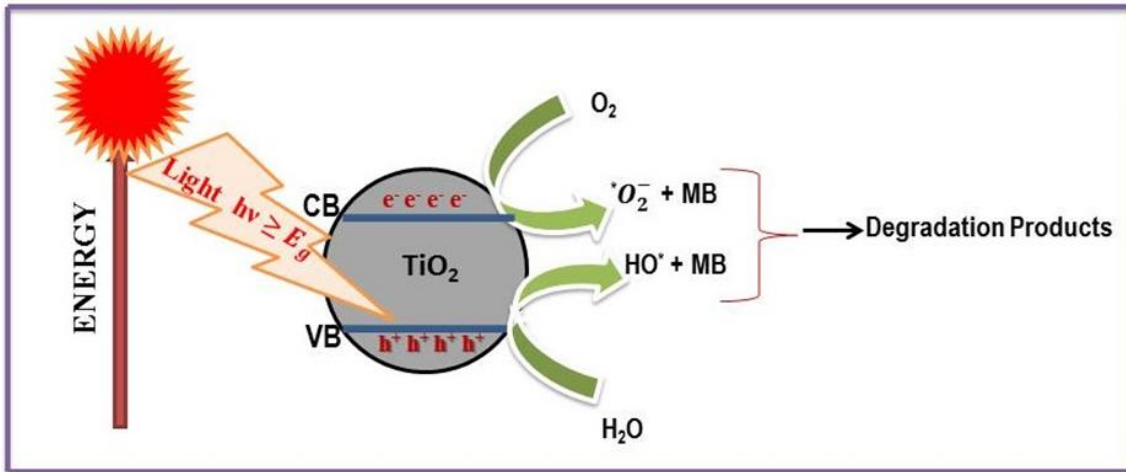


Fig. 12. Schematic representations of photocatalytic mechanism

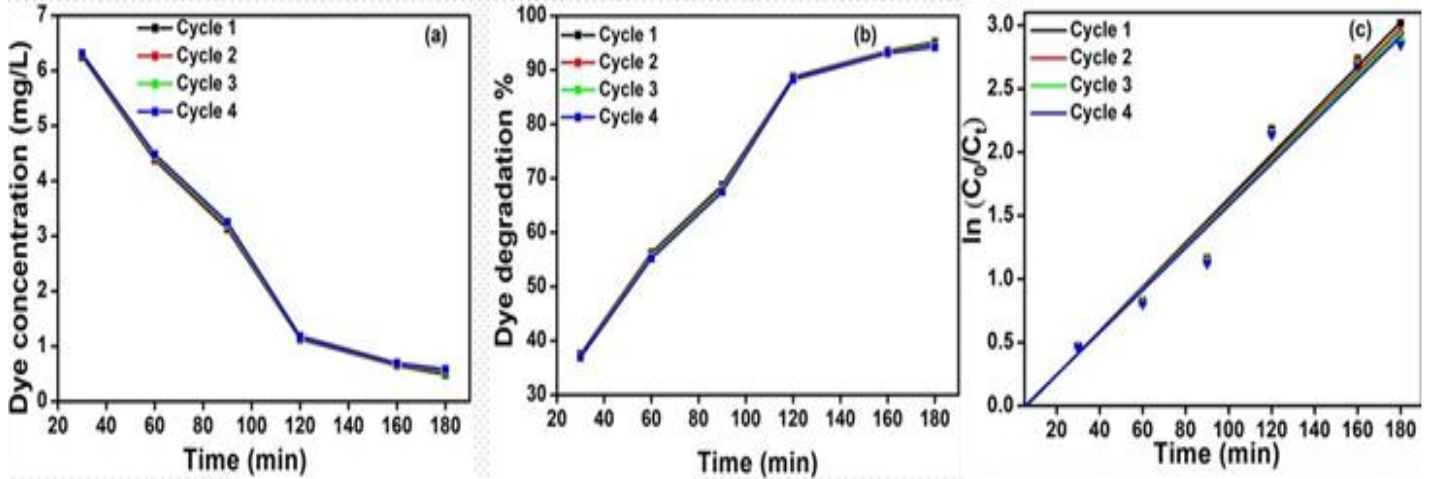


Fig. 13 (a-c). Photocatalytic activity of MB with TiO₂ nanoparticle: a) Time vs Dye concentration b) Time vs Dye degradation c) Time vs $\ln\left(\frac{C_0}{C_t}\right)$

Table 5. The values of k , R^2 , and $t_{1/2}$ of anatase TiO_2

Sample-TiO ₂	Rate constant kx10 ⁻² (min ⁻¹)	R ²	Half-life t _{1/2} (min)
Cycle 1	1.805	0.96918	38.40
Cycle 2	1.769	0.96745	39.16
Cycle 3	1.748	0.96564	39.66
Cycle 4	1.723	0.96238	40.23

The reaction rate levels off and becomes independent of 'C' at higher concentration ($C > 5.0$ mM), which is zero-order kinetics. The reaction rate is proportional to initial concentration, when the concentration below 1.0 mM and the reaction is first-order kinetics [73]. **Fig. 13c** shows the linear relationship between $\ln(C_0/C_t)$ and irradiation time. The results clearly indicate that the photodegradation of methylene blue (MB) follows first order kinetics. The rate constant was calculated for different cycles; 0.01805, 0.01769, 0.01748, and 0.01723 min⁻¹. The half-life time was obtained for first order kinetics using **equation (18)**. It is inferred that the rate constant decreases with different cycles. The higher rate constant and lower half life time for all cycles confirm that the prepared anatase TiO_2 nanomaterial is an effective catalyst [74,75]. The calculated rate constant and half- life time are given in **Table 5**. Besides, the crystallite size of the anatase TiO_2 also effectively impact on the degradation process. The relationship between first order rate constant and particle size is given in the **equation (19)**. The mathematical relation of half- life time with crystallite size can be obtained by substituting **equation (19)** in **equation (18)**, as shown in **equation (20)**. **Fig. 14** (a-b) shows the first order rate constant and half-life time with different crystallite sizes. The obtained result confirms that when crystallite size increases, rate constant decreases and half life time tends to increase. It is found that the degradation process is higher for smaller crystallite size [75].

$$t_{1/2} = \frac{0.693}{K_r} \quad (18)$$

$$K = -0.064 \ln(D) + 0.260 \quad (19)$$

$$t'_{1/2} = \frac{0.693}{0.064 \ln(D) + 0.260} \quad (20)$$

The results obtained in the present study are in good agreement with earlier reports (**Table 6**) [74,76,77], and endorses that the TiO_2 nanoparticles can be used as an effective photocatalyst for the degradation of methylene blue dye.

4. Conclusions

In this study, anatase- TiO_2 with tetragonal structure was synthesized by the sol-gel method. The structural and optical properties were analysed using various

characterization techniques, such as XRD, FESEM, UV-Vis, Raman, FTIR, and DLS. The crystallite size was calculated using Scherrer formula, the obtained average crystallite size is 16.81 nm. In addition, various structural and surface parameters were calculated using XRD data such as dislocation density, lattice constants, interplanar spacing, unit cell volume, density, number of unit cells in a particle, strain, specific surface area and porosity. The inter relation between crystallite size and strain were analysed using the W-H model. The UV-Vis study gives the absorption spectrum and band gap. The band gap value calculated using Tauc plot is 3.18 eV. The stretching modes of Ti and O atoms were obtained from Raman study and the characteristic peak of TiO_2 nanoparticles was found at 140 cm⁻¹. The FTIR analysis was done to identify the presence of functional groups and oxides in the prepared nano structure and the characteristic peak of anatase TiO_2 was obtained at 652.11 cm⁻¹. The degradation of MB dye was investigated with anatase TiO_2 . The calculated rate constant and half life time reveal the enhanced photodegradation of MB dye with prepared anatase TiO_2 as catalyst.

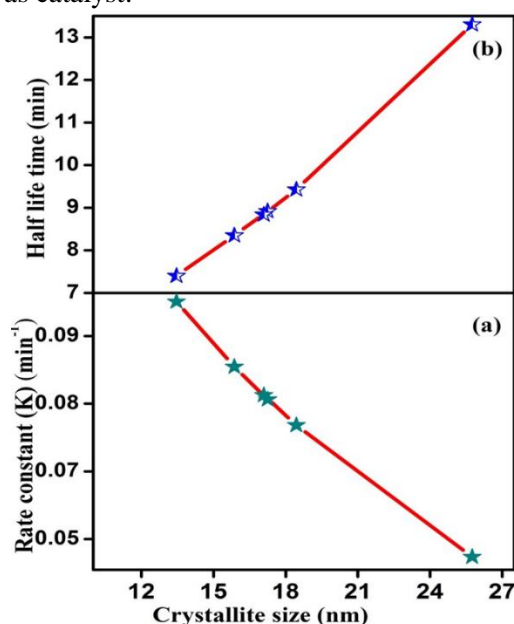


Fig. 14. Degradation analysis: a) Crystallite size vs Rate constant b) Crystallite size vs Half life time

Table 6. Comparison table of the rate constant (K_{app}) and Half- life time ($t_{1/2}$)

Rate constant K_{app} (min ⁻¹)	Half-life time $t_{1/2}$ (min)	References
0.0074	93.65	[59]
0.0080	86.63	[60]
0.0098	70.71	[61]
0.0023	301.30	[62]
0.0035	198	[63]
0.0180	38.5	[Present work]

Acknowledgements

One of the authors B. Manikandan thanks University Grants Commission, India for the financial support through UGC-RGNFD, Award letter No: F./2013-14/RGNF-2013-14D-OBC-TAM-56670; Dt: 30-10-2013.

References

- [1] S. Senbari and A. Nezamzadeh-Ejhi, *J. Mol. Liq.* 257 (2018) 173–183.
- [2] H. Zabihi-Mobarakeh and A. Nezamzadeh-Ejhi, *J. Ind. Eng. Chem.* 26 (2015) 315–321.
- [3] N. Arabpour and A. Nezamzadeh-Ejhi, *Mater. Sci. Semicond. Process.* 31 (2015) 684–692.
- [4] A. Nezamzadeh-Ejhi and H. Zabihi-Mobarakeh, *J. Ind. Eng. Chem.* 20 (2014) 1421–1431.
- [5] K. Nakata and A. Fujishima, *J. Photochem. Photobiol. C Photochem. Rev.* 13 (2012) 169–189.
- [6] J. Yu and M. Jaroniec, *Appl. Surf. Sci.* 319 (2014) 1.
- [7] M. El-Kemary, N. Nagy and I. El-Mehasseb, *Mater. Sci. Semicond. Process.* 16 (2013) 1747–1752.
- [8] A. C. Gandhi, H. Y. Cheng, Y. M. Chang and J. G. Lin, *Mater. Res. Express.* 3 (2016) 035017.
- [9] W. L. Kwong, H. Qiu, A. Nakaruk, P. Koshy and C. C. Sorrell, *Energy Procedia.* 34 (2013) 617–626.
- [10] H. Zhang, G. Chen and D. W. Bahnemann, *J. Mater. Chem.* 19 (2009) 5089–5121.
- [11] E. Thamarai Selvi and S. Meenakshi Sundar, *Mater. Res. Express.* 4 (2017) 075903.
- [12] Q. Lu, Z. Lu, Y. Lu, L. Lv, Y. Ning, H. Yu, Y. Hou and Y. Yin, *Nano Lett.* 13 (2013) 5698–5702.
- [13] M. R. Hoffmann, S. T. Martin, W. Choi and D. W. Bahnemann, *Chem. Rev.* 95 (1995) 69–96.
- [14] X. Lü, B. Xia, C. Liu, Y. Yang and H. Tang, *J. Nanomater.* 2016 (2016) 1–3.
- [15] R. S. Dariani, A. Esmaeili, A. Mortezaali and S. Dehghanpour, *Optik (Stuttg.)* 127 (2016) 7143–7154.
- [16] W. Chen, Q. Kuang, Q. Wang and Z. Xie, *RSC Adv.* 5 (2015) 20396–20409.
- [17] Y. Bai, I. Mora-Seró, F. De Angelis, J. Bisquert and P. Wang, *Chem. Rev.*, 114 (2014) 10095–10130.
- [18] I. Sopyan and N. Hafizah, *Int. J. Photoenergy.* 2009 (2009) 1–8.
- [19] J. Bai and B. Zhou, *Chem. Rev.* 114 (2014) 10131–10176.
- [20] J. Fan, Z. Li, W. Zhou, Y. Miao, Y. Zhang, J. Hu and G. Shao, *Appl. Surf. Sci.* 319 (2014) 75–82.
- [21] S. M. Gupta and M. Tripathi, *Chinese Sci. Bull.* 56 (2011) 1639–1657.
- [22] G. Strnad, C. Petrovan, O. Russu and L. Jakab-Farkas, *IOP Conf. Ser. Mater. Sci. Eng.* 161 (2016) 012051.
- [23] A. Nezamzadeh-Ejhi and M. Khorsandi, *J. Hazard. Mater.* 176 (2010) 629–637.
- [24] Y. S. Chang, M. Choi, M. Baek, P. Y. Hsieh, K. Yong and Y. J. Hsu, *Appl. Catal. B Environ.* 225 (2018) 379–385.
- [25] Y. H. Chiu, T. H. Lai, M. Y. Kuo, P. Y. Hsieh and Y. J. Hsu, *APL Mater.* 7 (2019) 080901.
- [26] P. Y. Hsieh, J. Y. Wu, T. F. M. Chang, C. Y. Chen, M. Sone and Y. J. Hsu, *Arab. J. Chem.* 13 (2020) 8372–8387.
- [27] T. P. Nguyen, D. L. T. Nguyen, V. H. Nguyen, T. H. Le, D. V. N. Vo, Q. T. Trinh, S. R. Bae, S. Y. Chae, S. Y. Kim and Q. Van Le, *Nanomaterials.* 10 (2020) 1–24.
- [28] Y. H. Chiu and Y. J. Hsu, *Nano Energy.* 31 (2017) 286–295.
- [29] Y. Wang, T. Wu, Y. Zhou, C. Meng, W. Zhu and L. Liu, *Sensors.* 17 (9) (2017) 1971.
- [30] A. Sharma, R. K. Karn and S. K. Pandiyan, *J. Basic Appl. Eng. Res.* 1 (2014) 1–5.
- [31] Y. Lan, Y. Lu and Z. Ren, *Nano Energy.* 2 (2013) 1031–1045.
- [32] G. Mattioli, A. Amore Bonapasta, D. Bovi and P. Giannozzi, *J. Phys. Chem. C.* 118 (2014) 29928–29942.
- [33] M. M. Momeni, *Bull. Mater. Sci.* 39 (2016) 1389–1395.
- [34] S. Gupta and M. Tripathi, *Open Chem.* 10(2) (2012) 279–294.
- [35] R. Liu, H. S. Wu, R. Yeh, C. Y. Lee and Y. Hung, *Int. J. Photoenergy.* 2012 (2012) 1–7.
- [36] Sirajudheen P, gireesh V, Sanoop K B, *Int. J. Adv. Mater Sci Eng.* 4 (2015) 33–39.
- [37] H.-Y. Lee and G. M. Kale, *Int. J. Appl. Ceram. Technol.* 5 (2008) 657–665.
- [38] S. Gayathri, P. Jayabal and V. Ramakrishnan, *AIP Conf. Proc.* 1665 (2015) 120025.
- [39] G. L. Li and G. H. Wang, *Nanostructured Mater.* 11 (1999) 663–668.
- [40] Y. T. Prabhu, K. V. Rao, V. S. S. Kumar and B. S. Kumari, *World J. Nano Sci. Eng.* 04 (2014) 21–28.
- [41] R. A. Caruso and M. Antonietti, *Chem. Mater.* 13 (2001) 3272–3282.
- [42] M. F. Goes, M. A. Sinhoreti, S. Consani and M. A. Silva, *Braz. Dent. J.* 9 (1998) 3–10.
- [43] G. Solero, *Nanosci. Nanotechnol.* 7 (2017) 21–25.
- [44] M. Niederberger, *Acc. Chem. Res.* 40 (2007) 793–800.
- [45] M. Gratzel, *J. Sol-Gel Sci. Technol.* 22 (2001) 7–13.
- [46] E. Asikuzun and O. Ozturk, *J. Mater. Sci. Mater. Electron.* 29 (2018) 7971–7978.
- [47] H. M. Chenari, C. Seibel, D. Hauschild, F. Reinert and H. Abdollahian, *Mater. Res* 19 (2016) 1319–1323.
- [48] B. Manikandan, T. Endo, S. Kaneko, K. R. Murali and R. John, *J. Mater. Sci. Mater. Electron.* 29 (2018) 9474–9485.
- [49] K. A. Aly, N. M. Khalil, Y. Algamil and Q. M. A. Saleem, *Mater. Chem. Phys.* 193 (2017) 182–188.
- [50] M. M. El-Nahass, M. H. Ali and A. El-Denglawey, *Trans. Nonferrous Met. Soc. China.* 22 (2012) 3003–3011.
- [51] A. Khorsand Zak, W. H. Abd. Majid, M. E. Abrishami and R. Yousefi, *Solid State Sci.* 13 (2011) 251–256.
- [52] M. R. Mohammadi, M. C. Cordero-Cabrera, M. Ghorbani and D. J. Fray, *J. Sol-Gel Sci. Technol.* 40 (2006) 15–23.
- [53] R. Sivakami, S. Dhanuskodi and R. Karvembu, *Spectrochim. Acta - Part A Mol. Biomol. Spectrosc.* 152 (2016) 43–50.
- [54] S. Bagheri, K. Shameli, S. Bee and A. Hamid, *J. Chem.* 2013 (2013) 1–5.
- [55] P. Bindu and S. Thomas, *J. Theor. Appl. Phys.* 8 (2014) 123–134.

- [56] N. Omrani and A. Nezamzadeh-Ejhieh, *Sep. Purif. Technol.* 235 (2020) 116228.
- [57] S. Venkatachalam, H. Hayashi, T. Ebina and H. Nanjo, *Optoelectron. - Adv. Mater. Devices.* (2013) 115-136.
- [58] A. Taherniya and D. Raoufi, *Semicond. Sci. Technol.* 31 (2016) 125012.
- [59] R. J. Alvaro, N. D. Diana and A. M. María. *Contemp. Eng. Sci.* 10 (2017) 1539–1549.
- [60] P. Chantes, C. Jarusutthirak and S. Danwittayakul. Int. Conf. on Biological, *Environ. Food Eng.* (2015) 15-16.
- [61] M. Vahtrus, A. Šutka, S. Vlassov, A. Šutka, B. Polyakov, R. Saar, L. Dorogin and R. Löhmus, *Mater. Charact.* 100 (2015) 98–103.
- [62] S. Dianat, *Iran. J. Catal.* 8 (2018) 121–132.
- [63] T. A. Egerton and I. R. Tooley, *Int. J. Cosmet. Sci.* 36 (2014) 195–206.
- [64] S. K. Gupta, R. Desai, P. K. Jha, S. Sahoo and D. Kirin, *J. Raman Spectrosc.* 41 (2009) 350–355.
- [65] T. Ohsaka, F. Izumi and Y. Fujiki, *J. Raman Spectrosc.* 7 (2018) 321–324.
- [66] M. A. Ahmed, E. E. El-Katori and Z. H. Gharni, *J. Alloys Compd.* 553 (2013) 19–29.
- [67] J. Zhang, P. Zhou, J. Liu and J. Yu, *Phys. Chem. Chem. Phys.* 16 (2014) 20382–20386.
- [68] R. Zuo, G. Du, W. Zhang, L. Liu, Y. Liu, L. Mei and Z. Li, *Adv. Mater. Sci. Eng.* 2014 (2014) 170148.
- [69] A. Giwa, P. O. Nkeonye, K. A. Bello and K. A. Kolawole, *J. Environ. Prot. (Irvine, Calif).* 03 (2012) 1063–1069.
- [70] N. Xu, Z. Shi, Y. Fan, J. Dong, J. Shi and M. Z.-C. Hu, *Ind. Eng. Chem. Res.* 38 (1999) 373–379.
- [71] D. M. de los Santos, J. Navas, T. Aguilar, A. Sánchez-Coronilla, C. Fernández-Lorenzo, R. Alcántara, J. C. Piñero, G. Blanco and J. Martín-Calleja, *Beilstein J. Nanotechnol.* 6 (2015) 605–616.
- [72] N. Omrani, A. Nezamzadeh-Ejhieh and M. Alizadeh, *Desalin. Water Treat.* 162 (2019) 290–302.
- [73] A. Nezamzadeh-Ejhieh and S. Hushmandrad, *Appl. Catal. A Gen.* 388 (2010) 149–159.
- [74] A. Kumar and G. Pandey, *JOJ Material Sci.* 2(5) (2017) 555596.
- [75] C. Yang, M. Zhang, W. Dong, G. Cui, Z. Ren and W. Wang, *PLoS One.* 12 (2017) e0174104.
- [76] M. Z. Bin Mukhlish, F. Najnin, M. M. Rahman and M. J. Uddin, *J. Sci. Res. J. Sci. Res.* 5(2) (2013) 301-314.
- [77] R. S. Dassanayake, E. Rajakaruna and N. Abidi, *J. Appl. Polym. Sci.* 45908 (2018) 1-10.